Published in final edited form as:
*IEEE Trans Biomed Eng*. 2011 November ; 58(11): 3121–3129. doi:10.1109/TBME.2011.2162514.

# Removal of spurious coherence in MEG source-space coherence analysis

**Kensuke Sekihara**[1], **Julia Owen**[2], **Stephan Trisno**[2], and **Srikantan S. Nagarajan**[2]

[1]Department of Systems Design and Engineering, Tokyo Metropolitan University, Asahigaoka 6-6, Hino, Tokyo 191-0065, Japan

[2]Biomagnetic Imaging Laboratory, Department of Radiology, University of California, San Francisco, 513 Parnassus Avenue, S362 San Francisco, CA 94143, USA

## Abstract

Lately, source-space coherence analysis has been applied to estimate functional connectivity using MEG/EEG data. Source space analysis involves solving the inverse problem, estimating the time courses of specific brain regions, and then examining the coherence across the estimated time courses. However, source-space coherence analysis is confounded by the leakage properties of the inverse algorithm, as manifested by a large seed peak (seed blur) in the resulting coherence images. This seed peak often obscures important details of brain interactions. This paper proposes the use of the imaginary part of the coherence to remove the spurious coherence caused by the leakage of an imaging algorithm. We present a theoretical analysis which explains how the use of imaginary part can remove this spurious coherence. We then present results of computer simulations and experiments using resting-state MEG data which demonstrate the validity of our analysis.

### Keywords

functional connectivity; coherence analysis; magnetoencephalography; leakage of imaging algorithm

## 1 Introduction

There has been tremendous interest in estimating the functional connectivity among neuronal oscillations across brain regions based on electromagnetic measurements such as magnetoencephalography (MEG) and electroencephalography (EEG). Since brain synchronous activities generally occur within a millisecond temporal scale, high temporal resolution of MEG and EEG makes these methods to be well suited for analyzing brain interactions. However, prior studies using EEG or MEG have largely employed sensor space analysis, in which brain interactions have been analyzed using raw sensor recordings [1, 2, 3]. In sensor space analysis, the field-spread across many sensors from a single brain region

Corresponding author: Kensuke Sekihara Ph.D., Department of Systems Design and Engineering, Tokyo Metropolitan University, Asahigaoka 6-6, Hino, Tokyo 191-0065, Japan, Tel:81-42-585-8642, Fax:81-42-585-8642, ksekiha@cc.tmit.ac.jp.

leads to uncertainties in interpreting the estimation results of brain interactions, as pointed out in [4].

Recently, a number of studies have begun to use source space analysis, which involves solving the inverse problem, estimating the time-course of specific brain regions, and examining the coherence across these estimated time courses [4, 5, 6, 7, 8]. Although a certain degree of inaccuracy exists in the source inversion process, the source-space analysis has the potential of providing more accurate information regarding which brain regions are functionally coupled.

Either in sensor- or source-space analysis, some kind of a measure for the interaction must be computed. Among existing measures, a widely-used, representative measure is coherence [9, 5, 6, 7, 10, 11]. In source-space coherence analysis, a typical procedure involves first setting a reference point called “the seed point” and computing coherence between the estimated time courses from the seed point and from another voxel locations, referred to as “the target location” in this paper. By scanning the target location, three-dimensional mapping of source coherence can be obtained, i.e., source coherence imaging can be performed.

A serious problem in source-coherence imaging arises from the spurious coherence caused by the leakage of an inverse algorithm, and such leakages are, to a greater or lesser extent, inevitable in any inverse algorithm [12]. A representative example of such spurious coherence is an artifact called the seed peak (or the seed blur), which is a peak located at the seed location in a coherence image. Quite often, the seed peak dominates resultant coherence images, and obscures important details of brain interactions. Examples of such seed peaks are shown in our computer simulation and experiments using the resting-state MEG data.

To remove such spurious coherence, this paper proposes the use of only the imaginary part of coherence. The use of imaginary coherence was originally proposed by Nolte *et al.* [13] to remove the spurious coherence caused by the volume conduction in EEG sensor-space coherence analysis. Imaginary coherence has already been applied to MEG source-space connectivity analysis, and clinical evaluations on the estimated results of functional connectivity have been reported for schizophrenia patients [14] and for brain tumor patients [7, 15]. In these reports, however, the primary scopes have been the clinical evaluations of the connectivity results and no rigorous arguments have yet been presented as to why the imaginary coherence was used in the first place.

This paper, therefore, presents rigorous arguments on why imaginary coherence offers a better measure. Detailed theoretical analysis is presented in Section 2 which explains how the use of the imaginary part can remove the spurious coherence caused by the leakage of source imaging algorithms. The validity of the analysis is then demonstrated by our computer simulation in Section 3 and by experiments using resting-state MEG data in Section 4.

## 2 Method

### 2.1 Source-space coherence analysis

The source-space coherence analysis requires two-step procedures. In the first step, voxel time courses are estimated using one of the available inverse algorithms. In the second step, the coherence measure is computed using the voxel time courses estimated in the first step. Here, coherence is computed between the time courses from the seed voxel and from the target voxel. Let us define the time course from the seed voxel as $u_S(t)$ and the time course from the target voxel as $u_T(t)$, and let the spectra of the seed and the target voxels be $\sigma_S(f)$ and $\sigma_T(f)$, respectively, such that

$$\sigma_S(f)=\int_{-\infty}^{\infty} u_S(t)e^{-2\pi f t}dt, \quad (1)$$

and

$$\sigma_T(f)=\int_{-\infty}^{\infty} u_T(t)e^{-i2\pi f t}dt. \quad (2)$$

The coherence $\eta(f)$ is obtained by computing the correlation of these spectra, such that

$$\eta(f)=\frac{\langle \sigma_T(f)\sigma_S^*(f)\rangle}{\sqrt{\langle|\sigma_T(f)|^2\rangle\langle|\sigma_S(f)|^2\rangle}}, \quad (3)$$

where the superscript $^*$ indicates the complex conjugate, and the bracket $\langle\cdot\rangle$ indicates the ensemble average. In practical applications, this ensemble average is computed by averaging across multiple trials[*].

It is apparent from Eq. (3) that, if the seed and target spectra contain common components that do not result from true brain interactions, the coherence may contain spurious components. When coherence is computed using the estimated voxel time courses, the leakage of an imaging algorithm is a major source of such spurious coherence. An artifact called the seed peak (or the seed blur) is a typical example of such spurious coherence.

### 2.2 Seed-signal regression analysis

To remove such leakage influence in source coherence imaging, we propose the use of only the imaginary part of coherence. In Section 2, we explain why the use of the imaginary coherence can remove the leakage effects of inverse algorithms. For this explanation, we first introduce seed-signal regression analysis which has led us to a new insight on the use of the imaginary part of coherence.

That is, we try to regress $\sigma_T(f)$ using $\sigma_S(f)$, such that

[*]When only a single continuous data set is measured, the single data set is divided into many portions and coherence is obtained by averaging across these portions.

$$\sigma_T(f)=\alpha\sigma_S(f)+v(f), \quad (4)$$

where $\alpha$ is a real-valued multiplicative constant, and $v(f)$ is a residual signal. Namely, we express the target spectrum $\sigma_T(f)$ as a summation of a scaled replica of the seed spectrum $\alpha\sigma_S(f)$ and the residual $v(f)$. The optimum value for $\alpha$ is determined using

$$\hat{\alpha}=\arg\min_{\alpha}\langle|\sigma_T(f)-\alpha\sigma_S(f)|^2\rangle. \quad (5)$$

Noting that $\alpha$ is real, we have

$$\langle|\sigma_T(f)-\alpha\sigma_S(f)|^2\rangle=\alpha^2\langle|\sigma_S(f)|^2\rangle-2\alpha\Re[\langle\sigma_T(f)\sigma_S^*(f)\rangle]+\langle|\sigma_T(f)|^2\rangle, \quad (6)$$

where $\Re[\cdot]$ indicates the real part.

The optimum estimate of $\alpha$ is thus derived as

$$\hat{\sigma}=\frac{\Re[\langle\sigma_T(f)\sigma_S^*(f)\rangle]}{\langle|\sigma_S(f)|^2\rangle}, \quad (7)$$

and the residual is expressed as

$$v(f)=\sigma_T(f)-\hat{\alpha}\sigma_S(f)=\sigma_T(f)-\frac{\Re[\langle\sigma_T(f)\sigma_S^*(f)\rangle]}{\langle|\sigma_S(f)|^2\rangle}\sigma_S(f). \quad (8)$$

The cross spectrum between the residual and seed signals is

$$\begin{aligned}\langle v(f)\sigma_S(f)^*\rangle&=\langle\sigma_T(f)\sigma_S(f)^*\rangle-\frac{\Re[\langle\sigma_T(f)\sigma_S(f)^*\rangle]}{\langle|\sigma_S(f)|^2\rangle}\langle|\sigma_S(f)|^2\rangle\\&=\langle\sigma_T(f)\sigma_S(f)^*\rangle-\Re[\langle\sigma_T(f)\sigma_S(f)^*\rangle]=\Im[\langle\sigma_T(f)\sigma_S(f)^*\rangle],\end{aligned} \quad (9)$$

where $\Im[\cdot]$ indicates the imaginary part. The equation above shows that the cross spectrum between $v(f)$ and $\sigma_S(f)$ is equal to the imaginary part of the cross spectrum between $\sigma_T(f)$ and $\sigma_S(f)$.

## 2.3 Leakage effects of imaging algorithms

**2.3.1 Leakage effects in the magnitude coherence—**Based on the arguments above, we show that the imaginary part of coherence can be used to remove the spurious coherence. The estimated source time courses at the seed and the target voxels, $\hat{u}_S(t)$ and $\hat{u}_S(t)$, can generally be expressed as

$$\hat{u}_S(t)=u_S(t)+d_1u_T(t)+c_S(t), \quad (10)$$

and

$$\hat{u}_T(t)=u_T(t)+d_2u_S(t)+c_T(t). \quad (11)$$

Recall that $u_S(t)$ and $u_T(t)$ are the true source time courses of the seed and the target locations†. In the above equations, $d_1u_T(t)$ indicates the leakage of the target signal in the estimated seed signal, and $d_2u_S(t)$ indicates the leakage of the seed signal in the estimated target signal. The real-valued constants $d_1$ and $d_2$ express the relative amount of these leakages.

In the equations above, $c_S(t)$ and $c_T(t)$ express the interference terms, which may include the leakage from other sources, contributions from external disturbances, and the influence of the sensor noise. In the following arguments, we ignore $c_S(t)$ and $c_T(t)$ for simplicity. The influence of these interference terms may be considered separately from the influence of the leakage terms. A brief discussion on these interference terms is presented in Section 5. Thus, the estimated spectra at the seed and target voxels, $\hat{\sigma_S}(f)$ and $\hat{\sigma_T}(f)$, are expressed as

$$\hat{\sigma}_S=\sigma_S+d_1\sigma_T, \quad (12)$$

and

$$\hat{\sigma}_T=\sigma_T+d_2\sigma_S, \quad (13)$$

where we omit the explicit notation of $(f)$ for simplicity.

The magnitude coherence between the seed and the target voxels is derived by substituting Eqs. (12) and (13) into (3), and is expressed as

$$|\hat{\eta}|=\left|\frac{\langle\hat{\sigma}_T\hat{\sigma}_S^*\rangle}{\sqrt{\langle|\hat{\sigma}_T|^2\rangle\langle|\hat{\sigma}_S|^2\rangle}}\right| =\frac{|\langle\sigma_T\sigma_S^*\rangle+d_1\langle|\sigma_T|^2\rangle+d_2\langle|\sigma_S|^2\rangle+d_1d_2\langle\sigma_S\sigma_T^*\rangle|}{\sqrt{(\langle|\sigma_S|^2\rangle+d_1^2\langle|\sigma_T|^2\rangle+2d_1\Re[\langle\sigma_T\sigma_S^*\rangle])\,(\langle|\sigma_T|^2\rangle+d_2^2\langle|\sigma_S|^2\rangle+2d_2\Re[\langle\sigma_T\sigma_S^*\rangle])}}. \quad (14)$$

Therefore, even when there is no true source interaction, i.e., even when $\langle\sigma_T\sigma_S^*\rangle=0$ and $\langle\sigma_S\sigma_T^*\rangle=0$, $|\hat{\eta}|$ has a non-zero value, which is equal to

$$|\hat{\eta}|=\frac{|d_1\langle|\sigma_T|^2\rangle+d_2\langle|\sigma_S|^2\rangle|}{\sqrt{(\langle|\sigma_S|^2\rangle+d_1^2\langle|\sigma_T|^2\rangle)\,(\langle|\sigma_T|^2\rangle+d_2^2\langle|\sigma_S|^2\rangle)}}. \quad (15)$$

Namely, the spurious coherence is caused by the auto-correlation between $\sigma_S$ and its leakage $d_2\sigma_S$, and by the auto-correlation between $\sigma_T$ and its leakage $d_1\sigma_T$.

†In this paper, the estimated values are indicated by ^ to distinguish their true values.

**2.3.2 Leakage effects in the imaginary part of the cross spectrum—**We next show that the imaginary part of the cross spectrum $\langle \hat{\sigma}_T \hat{\sigma}_S^* \rangle$ does not contain these auto-correlation components. To show this, we rewrite Eq. (13) as

$$\hat{\sigma}_T = (1 - d_1 d_2)\sigma_T + d_2 \hat{\sigma}_S. \quad (16)$$

According to Eq. (9), computing the imaginary part of $\langle \hat{\sigma}_T \hat{\sigma}_S^* \rangle$ is equivalent to computing $\langle v \hat{\sigma}_S^* \rangle$, where

$$v = \hat{\sigma}_T - \hat{\alpha}\hat{\sigma}_S, \quad (17)$$

and

$$\hat{\alpha} = \frac{\Re[\langle \hat{\sigma}_T \hat{\sigma}_S^* \rangle]}{\langle |\hat{\sigma}_S|^2 \rangle}. \quad (18)$$

Substituting Eq. (16) into (18), we obtain

$$\hat{\alpha} = d_2 + (1 - d_1 d_2)\frac{\Re[\langle \sigma_T \hat{\sigma}_S^* \rangle]}{\langle |\hat{\sigma}_S|^2 \rangle}. \quad (19)$$

Substituting Eqs. (16) and (19) into Eq. (17), we then obtain

$$v = (1 - d_1 d_2) \left[ \sigma_T - \frac{\Re[\langle \sigma_T \hat{\sigma}_S^* \rangle]}{\langle |\hat{\sigma}_S|^2 \rangle} \hat{\sigma}_S \right], \quad (20)$$

and thus, we have

$$\langle v \hat{\sigma}_S^* \rangle = (1 - d_1 d_2)\,[\langle \sigma_T \hat{\sigma}_S^* \rangle - \Re[\langle \sigma_T \hat{\sigma}_S^* \rangle]] = (1 - d_1 d_2)\Im[\langle \sigma_T \hat{\sigma}_S^* \rangle]. \quad (21)$$

Using Eq. (12), we have the relationship, $\langle \sigma_T \hat{\sigma}_S^* \rangle = \langle \sigma_T \sigma_S^* \rangle + d_1 \langle |\sigma_T|^2 \rangle$, and we obtain

$$\Im[\langle \sigma_T \hat{\sigma}_S^* \rangle] = \Im[\langle \sigma_T \sigma_S^* \rangle] + d_1 \Im[\langle |\sigma_T|^2 \rangle] = \Im[\langle \sigma_T \sigma_S^* \rangle], \quad (22)$$

since $\Im[\langle |\sigma_T|^2 \rangle] = 0$. We thereby derive

$$\Im[\langle \hat{\sigma}_T \hat{\sigma}_S^* \rangle] = \langle v \hat{\sigma}_S^* \rangle = (1 - d_1 d_2)\Im[\langle \sigma_T \sigma_S^* \rangle]. \quad (23)$$

The above equation indicates that, aside from the multiplicative constant, the imaginary part of the cross spectrum between the seed and target voxels is equal to $\Im[\langle \sigma_T \sigma_S^* \rangle]$, which is the imaginary part of the true cross spectrum.

**2.3.3 Leakage effects in the imaginary part of coherence—**To compute coherence, the cross spectrum $\langle \hat{\sigma}_T \hat{\sigma}_S^* \rangle$ is normalized by $\sqrt{\langle |\hat{\sigma}_T|^2 \rangle \langle |\hat{\sigma}_S|^2 \rangle}$. Using Eqs. (12) and (13), we derive

$$\langle |\hat{\sigma}_S|^2 \rangle = \langle |\sigma_S|^2 \rangle + d_1^2 \langle |\sigma_T|^2 \rangle + 2d_1 \Re[\langle \sigma_T \sigma_S^* \rangle], \quad (24)$$

and

$$\langle |\hat{\sigma}_T|^2 \rangle = \langle |\sigma_T|^2 \rangle + d_2^2 \langle |\sigma_S|^2 \rangle + 2d_2 \Re[\langle \sigma_T \sigma_S^* \rangle]. \quad (25)$$

Thus, we obtain the imaginary part of the estimated coherence $\Im(\hat{\eta})$ as

$$\begin{aligned} \Im(\hat{\eta}) &= \Im\left[\frac{\langle \hat{\sigma}_T \hat{\sigma}_S^* \rangle}{\sqrt{\langle |\hat{\sigma}_T|^2 \rangle \langle |\hat{\sigma}_S|^2 \rangle}}\right] \\ &= \frac{(1-d_1 d_2)\Im[\langle \sigma_T \sigma_S^* \rangle]}{\sqrt{(\langle |\sigma_S|^2 \rangle + d_1^2 \langle |\sigma_T|^2 \rangle + 2d_1 \Re[\langle \sigma_T \sigma_S^* \rangle])\,(\langle |\sigma_T|^2 \rangle + d_2^2 \langle |\sigma_S|^2 \rangle + 2d_2 \Re[\langle \sigma_T \sigma_S^* \rangle])}} \\ &= \Im(\eta) \frac{(1-d_1 d_2)}{\sqrt{\left(1 + d_1^2 \frac{\langle |\sigma_T|^2 \rangle}{\langle |\sigma_s|^2 \rangle} + 2d_1 \frac{\Re[\langle \sigma_T \sigma_S^* \rangle]}{\langle |\sigma_S|^2 \rangle}\right)\left(1 + d_2^2 \frac{\langle |\sigma_S|^2 \rangle}{\langle |\sigma_T|^2 \rangle} + 2d_2 \frac{\Re[\langle \sigma_T \sigma_S^* \rangle]}{\langle |\sigma_T|^2 \rangle}\right)}}, \end{aligned} \quad (26)$$

where $\Im(\eta)$ indicates the true value of the imaginary coherence, which is

$$\Im(\eta) = \frac{\Im[\langle \sigma_T \sigma_S^* \rangle]}{\sqrt{\langle |\sigma_T|^2 \rangle \langle |\sigma_S|^2 \rangle}}. \quad (27)$$

Equation (26) shows that when $\Im(\eta) = 0$, we have $\Im(\hat{\eta}) = 0$, indicating that no spurious coherence has been generated. However, Eq. (26) also indicates that the value of $\Im(\hat{\eta})$ differs from the true value $\Im(\eta)$. The difference depends on the amount of the leakage. When the leakage is large, i.e., when $d_1$ and $d_2$ are large, the estimated value of the imaginary coherence, $\Im(\hat{\eta})$, may differ considerably from the true value $\Im(\eta)$.

**2.3.4 Alternative normalization method—**The arguments in Section 2.2 suggest an alternative method of normalizing the cross spectrum. That is, since the relationship $\Im[\langle \hat{\sigma}_T \hat{\sigma}_S^* \rangle] = \langle v \hat{\sigma}_S^* \rangle$ holds except for scaling, we suggest normalization of $\Im[\langle \hat{\sigma}_T \hat{\sigma}_S^* \rangle]$ by $\sqrt{\langle |v|^2 \rangle \langle |\hat{\sigma}_S|^2 \rangle}$. Using Eq. (20), we obtain the relationship,

$$\langle |v|^2 \rangle \langle |\hat{\sigma}_S|^2 \rangle = (1-d_1 d_2)^2 [\langle |\sigma_T|^2 \rangle \langle |\hat{\sigma}_S|^2 \rangle - \Re[\langle \sigma_T \hat{\sigma}_S^* \rangle]^2]. \quad (28)$$

Using Eq. (12), we have

$$\Re[\langle \sigma_T \hat{\sigma}_S^* \rangle] = \Re[\langle \sigma_T \hat{\sigma}_S^* \rangle] + d_1 \langle |\sigma_T|^2 \rangle. \quad (29)$$

Therefore, substituting Eqs. (29) and (24) into (28), we derive

$$\langle |v|^2 \rangle \langle |\hat{\sigma}_S|^2 \rangle = (1-d_1 d_2)^2 [\langle |\sigma_T|^2 \rangle \langle |\hat{\sigma}_S|^2 \rangle - \Re[\langle \sigma_T \hat{\sigma}_S^* \rangle]^2]. \quad (30)$$

Using the above equation and Eq. (23), we further derive

$$\Im(\tilde{\eta}) = \frac{\Im[\langle \hat{\sigma}_T \hat{\sigma}_S^* \rangle]}{\sqrt{\langle |v|^2 \rangle \langle |\hat{\sigma}_S|^2 \rangle}} = \frac{\Im[\langle \sigma_T \sigma_S^* \rangle]}{\sqrt{\langle |\sigma_T|^2 \rangle \langle |\sigma_S|^2 \rangle - \Re[\langle \sigma_T \sigma_S^* \rangle]^2}} = \frac{\Im(\eta)}{\sqrt{1-\Re(\eta)^2}}, \quad (31)$$

where $\tilde{\eta}$ indicates the (modified) coherence with the proposed normalization, i.e., $\tilde{\eta} = \langle \hat{\sigma}_T \hat{\sigma}_S^* \rangle / \sqrt{\langle |v|^2 \rangle \langle |\hat{\sigma}_S|^2 \rangle}$. Equation (31) shows that, when $\Im(\eta) = 0$, we have $\Im(\tilde{\eta}) = 0$. Thus, $\Im(\tilde{\eta})$ does not contain the spurious coherence. Actually, it is clear that $\Im(\tilde{\eta})$ is free from the leakage influence, since the right-hand side of Eq. (31) does not contain the leakage constants $d_1$ and $d_2$. Although $\Im(\tilde{\eta})$ is different from the true value $\Im(\eta)$, the difference is generally small. For example, even when $\Re(\eta)$ is quite large as in when $\Re(\eta) = 0.5$, $1/\sqrt{1-\Re(\eta)^2}$ is then equal to 1.16, i.e., the scaling error is only 16% in this case.

## 3 Computer Simulation

### 3.1 Data generation

Computer simulations were performed to verify the results of the arguments in Section 2. In our simulations, we used a sensor alignment of the 275-sensor array from the Omega™ (VMS Medtech, Coquitlam, Canada) neuromagnetometer. A single vertical plane ($x$ = 0 cm) was assumed at the middle of the whole-head sensor array, and three sources were assumed to exist on this plane. The source-sensor configuration and the coordinate system are depicted in Fig. 1. The ($y$, $z$) coordinates of the three sources were (−1.0, 9.5) cm, (1.5, 10.0) cm, and (1.0, 7.5) cm, respectively.

Multiple-trial measurement was simulated, in which a total of 120-trial recordings were generated. Each trial consists of 600 time points where the sampling interval was assumed to be 2 ms. The time courses of the three sources had the same shape with different trial-to-trial time jitters. The time jitter between the first and second sources and the jitter between the second and the third sources were both generated using Gaussian random numbers with a standard deviation equal to 15 time points. The source time courses in the first three trials are shown in Fig. 2.

Defining the $j$th-source time course given as $u_j(t)$, the signal magnetic recordings $\boldsymbol{b}_s(t)$ were computed using

$$\boldsymbol{b}_s(t) = \sum_{j=1}^{3} A_j u_j(t) \boldsymbol{l}_j, \quad (32)$$

where $\boldsymbol{l}_j$ are the lead field vector of the $j$th source and $A_j$ is its amplitude. Here, the powers of the three sources were set equal in the sensor-domain, i.e., the relationship,

$$A_1^2\|\boldsymbol{l}_1\|^2=A_2^2\|\boldsymbol{l}_2\|^2=A_3^2\|\boldsymbol{l}_3\|^2,$$

held. The lead field was calculated using the spherical homogeneous conductor model [16] with the sphere origin set to (0, 0, 4) cm.

The simulated sensor recordings $\boldsymbol{b}(t)$ were generated by adding spontaneous MEG signal to the signal recordings $\boldsymbol{b}_s(t)$, such that,

$$\boldsymbol{b}(t)=\boldsymbol{b}_s(t)+\gamma\boldsymbol{b}_I(t), \quad (33)$$

where $\boldsymbol{b}_I(t)$ is the spontaneous MEG measured using the same 275 whole-head sensor array, and $\gamma$ is a constant that controls the signal-to-interference ratio (SIR) of the simulated sensor recordings. In this computer simulation, SIR was set equal to 4.0 and 0.25, where SIR is defined as the ratio of the average signal power $\langle\|\boldsymbol{b}_s(t)\|^2\rangle$ to the average interference power $\langle\|\boldsymbol{b}_I(t)\|^2\rangle$. Note that the coherence analysis is usually performed using non-averaged trial data. Therefore, an SIR of 4.0 is considered a significantly high SIR and the SIR of 0.25 is considered a practical SIR.

### 3.2 Source coherence imaging

The voxel time-course estimation was performed using the narrow-band adaptive spatial filter [12][17] with a data-covariance matrix obtained with a frequency band between 8 and 12 Hz. Reconstructed source power images on the plane $x$ = 0 cm are shown in Fig. 3 for both SIR cases. The reconstructed images show that the three sources are resolved for the both SIR cases. We then set a seed point at the location of the second source to compute coherence images. The seed point is marked by asterisks in Fig. 3. The resultant coherence images are shown in Fig. 4. In this figure, the upper panels ((a) and (b)) show the results for the case of the SIR equal to 4.0, and the lower panels ((c) and (d)) show the results for the case of the SIR equal to 0.25. Also, the left panels ((a) and (c)) show the magnitude coherence images and the right panels ((b) and (d)) show the imaginary coherence images. Here, the imaginary coherence is computed using Eq. (31).

When the SIR is equal to 4.0, i.e., when the SIR is very high, the magnitude coherence image (Fig. 3(a)) manages to show the first and the third sources, although a large seed peak exists at the second source location. That is, the two sources interacting with the second source can be observed in spite of the existence of the seed peak when the SIR is very high. In the imaginary coherence image (Fig. 3(b)), the intensity of the seed peak is much reduced, and the first and the second sources, which interact with the second source, are clearly shown.

When the SIR is equal to 0.25, the seed peak dominates and it obscures the other sources in the magnitude coherence image (Fig. 3(c)). Thus, it is difficult to obtain information on the

interacting sources from the magnitude coherence image. On the contrary, in the imaginary coherence image (Fig. 3(d)), the intensity of the seed peak is much reduced and the two interacting sources can clearly be observed. For both of the SIR cases, however, the seed peak is not completely eliminated in the imaginary coherence images, and regions near the seed location still show some non-zero coherence values. An argument on the cause of these small non-zero coherence values is presented in Section 5.

Next, we performed computer simulation in which no source activity existed at the seed location. Here, the first source was made inactive and the seed was set at the first source location. The results of the source power reconstruction in this case are shown in Fig. 5(a). The results contain the second and the third source but do not contain the first source. The seed location is indicated by the asterisk at the first source location. The magnitude-coherence image and the imaginary-coherence image are shown in Figs. 5(b) and (c). The magnitude-coherence image (Fig. 5(b)) shows a large blurred peak at the seed location, as if the large region surrounding the seed location is synchronously active. This large region represents the spurious coherence expressed in Eq. (15). The imaginary coherence image (Fig. 5(c)), however, shows no activity, the results clearly validating our arguments in Section 2.

## 4 Experiments with resting-state MEG data

We performed source coherence imaging using resting state MEG data. The data was acquired using a 275-channel CTF Omega 2000™ whole-head MEG system (VSM MedTech, Coquitlam, BC, Canada). When collecting the data, subjects laid down with their eyes closed, and 60-sec-long single continuous data sets were acquired with a 1200 Hz sampling rate. The single trial data was divided into 2-sec long trials with half overlap, resulting in a total of sixty trials.

In the first experiments, the voxel time-courses were estimated using a narrow-band adaptive spatial filter [12][17] with a frequency window (for the alpha band) between 9 and 11 Hz. The results of imaging experiments for two subjects are shown in Fig. 6 in which the results for one subject are shown in (a) and the results for the other subject are shown in (b). In the results from each subject, the reconstructed source power distribution is shown in the upper panels, the magnitude coherence image is shown in the middle panels, and the imaginary coherence image is shown in the bottom panels. The seed was set at the location having the maximum intensity of the reconstructed source distributions. The seed locations are indicated by asterisks.

The results from both of the two subjects show that the seed peaks dominate the magnitude coherence images. Thus, it is difficult to obtain any information on interacting brain activities in these magnitude coherence images. On the other hand, the imaginary coherence images show activities that are different from the seed activity and that are not found in the magnitude coherence images‡.

‡Although the physiological meaning of these activities in the imaginary coherence images has not yet been explored, we may interpret these activities as representing the default-mode brain network of healthy subjects [18].

We next performed imaging of source coherence between the left and the right primary motor cortices using the resting-state MEG data sets, which were acquired in exactly the same procedure as mentioned above. The voxel time courses were estimated using the narrow-band adaptive spatial filter with the frequency band tuned to the individual subjects' beta-band, which was approximately between 14 to 27 Hz. To obtain seed voxels in the left pre-central gyrus, we selected all the voxels labeled as the pre-central gyrus. These labels were obtained by normalizing the subjects MRI to the Montreal Neurological Institute (MNI) template brain. We then computed the centroid for these voxels and selected nine nearest voxels to the centroid, resulting in ten seed voxels in the left pre-central gyrus for each subject. The seed voxels for each individual subject are shown in the two right-hand-side columns of Fig. 7. The analysis was performed using the NUTMEG toolbox [19].

We then computed the magnitude and imaginary coherence between the seed voxels and the rest of the voxels in the brain, resulting in ten coherence images corresponding to ten seed voxels. The final coherence image was obtained by averaging those ten coherence images. The results are shown in Fig. 7 in which the two central columns show the magnitude coherence images, and the two right-hand-side columns show the imaginary coherence images. The results here show that the magnitude coherence images are dominated by the seed peaks. That is, for all three subjects, the peaks in the magnitude coherence images are located near the seed voxel and no other peaks are seen. On the contrary, the imaginary coherence images are able to detect the right motor cortex and show the connectivity between the left and right motor cortices in the beta band. The seed peaks that dominate the magnitude coherence images are not seen in the imaginary coherence images.

## 5 Discussion and summary

In the results of our computer simulation in Fig. 4, the seed peak is not completely removed in the imaginary coherence images, and regions near the seed location show some non-zero coherence values. These non-zero coherence values may arise because coherence was computed using sample averaging with a limited number of trials. We thus applied statistical thresholding using the surrogate-data bootstrapping method [20, 21] to check whether these non-zero coherence values were caused by the averaging with a limited sample size.

Here, two hundred sets of surrogate time courses were generated. The surrogate voxel time courses had the same power spectra as those of the original voxel time courses, but these surrogate voxel time courses were completely mutually incoherent, because the phase relationships were destroyed by multiplying random phases with the original voxel spectra. The null distribution was formed at each voxel using the two hundred coherence values computed using the two-hundred surrogate data sets. Maximum statistics were used to take the multiple comparisons into consideration [22, 23]. The statistical significance, which is the probability of a type one error, was set to 0.05.

In these procedures, the null distribution took the spurious coherence due to the averaging with a limited sample size into account. Thus, the non-zero coherence regions near the seed location in the imaginary coherence images was expected to be removed by this statistical thresholding. The statistically-thresholded coherence images are shown in Fig. 8. In the

thresholded imaginary coherence images (Fig. 8 (b) and (d)), the non-zero coherence regions around the seed location were removed, and only the regions that are interacting with the seed source appear. It should also be pointed out that the statistical thresholding cannot remove the seed peaks, which remain in the magnitude coherence images even after statistical thresholding.

In the analysis in Section 2, we ignored the interference terms $c_S(t)$ and $c_T(t)$. Here, we present a brief discussion on the influence of these interference terms and for this discussion, we use the expressions:

$$\hat{\sigma}_S = \overline{\sigma}_S + C_S, \quad \text{and} \quad \hat{\sigma}_T = \overline{\sigma}_T + C_T, \quad (34)$$

where we omit the explicit notation of ($f$) for simplicity. In the above expressions, $C_S(f)$ and $C_T(f)$ are the spectra of the interference terms $c_S(t)$ and $c_T(t)$, and $\overline{\sigma_S}$ and $\overline{\sigma_S}$ are the source spectra including the leakage terms, which are defined such that $\overline{\sigma_S} = \sigma_S + d_1\sigma_T$ and $\overline{\sigma_T} = \sigma_T + d_2\sigma_S$. We assume that the interference spectra are independent from the source spectra, i.e., that the relationships, $\langle \overline{\sigma}_T C_T^* \rangle = 0$, $\langle \overline{\sigma}_T C_S^* \rangle = 0$, $\langle \overline{\sigma}_S C_T^* \rangle = 0$, and $\langle \overline{\sigma}_S C_S^* \rangle = 0$, hold.

Then, using Eqs. (34), the cross-spectrum $\langle \overline{\sigma}_T \overline{\sigma}_S^* \rangle$ is expressed as

$$\langle \overline{\sigma}_T \overline{\sigma}_S^* \rangle = \langle \overline{\sigma}_T \overline{\sigma}_S^* \rangle + \langle C_T C_S^* \rangle, \quad (35)$$

where $\langle C_T C_S^* \rangle$ indicates the spurious component due to the interference terms. The above equation indicates that the interference terms cause the spurious component in a manner additive to the spurious component caused from the leakage terms.

Taking the imaginary part of both sides of Eq. (35), we derive

$$\Im[\langle \overline{\sigma}_T \overline{\sigma}_S^* \rangle] = \Im[\langle \overline{\sigma}_T \overline{\sigma}_S^* \rangle] + \Im[\langle C_T C_S^* \rangle], \quad (36)$$

where $\Im[\langle C_T C_S^* \rangle]$ is a spurious component in the imaginary part of cross spectrum. If $\langle C_T C_S^* \rangle$ is real-valued, we have $\Im[\langle \overline{\sigma}_T \overline{\sigma}_S^* \rangle] = \Im[\langle \overline{\sigma}_T \overline{\sigma}_S^* \rangle]$, and taking the imaginary part allows removal of this spurious component. However, to further investigate what scenarios make $\langle C_T C_S^* \rangle$ real-valued, we must take the property of inverse algorithms into consideration. Such investigation is currently undertaken and further results will be published in the near future.

It should be pointed out that using the imaginary part of coherence always underestimates connectivity. This fact is rather obvious in Eq. (9), which shows that the imaginary part of the cross correlation, $\Im[\langle \sigma_T(f)\sigma_S(f)^* \rangle]$, is equal to the cross correlation between the seed signal and the residual, $\langle v(f)\sigma_S(f)^* \rangle$. Here, since the residual $v(f)$ is obtained by subtracting $a\hat{\sigma}_S(f)$ from the target signal $\sigma_T(f)$, the imaginary coherence does not account for the auto-correlation between $\sigma_S(f)$ and a component represented by $a\hat{\sigma}_S(f)$ in the target signal. Thus, if such auto-correlation components exist in true brain interactions, taking imaginary part removes those components, together with the spurious components.

In summary, this paper proposes the use of the imaginary part of coherence to remove the spurious coherence caused by the leakage effects of source inverse algorithms. We have presented detailed theoretical analysis to show how the use of imaginary coherence can remove the spurious coherence. The analysis has been validated by computer simulations and experiments using resting-state MEG data.

## Acknowledgments

We would like to thank Sussane Honma and Anne Findlay for their help in measuring the resting-state MEG data. This work has been supported by Grants-in-Aid from the Ministry of Education, Science, Culture and Sports in Japan (20500394,22659210) to KS. This work has also been supported in part by grants from the National Institute of Health (R01-DC004855-01A1, R01-NS006435) to SN.

## References

1. Liu Z, Fukunaga M, de Zwart JA, Duyn JH. Large-scale spontaneous fluctuations and correlations in brain electrical activity observed with magnetoencephalography. NeuroImage. 2010; 51:102–111. [PubMed: 20123024]
2. Montez T, Poil S, Jones BF, Manshanden I, Verbunt JPA, van Dijk BW, Brussaard AB, van Ooyen A, Stam CJ, Scheltens P, Linkenkaer-Hansen K. Altered temporal correlations in parietal alpha and prefrontal theta oscillations in early stage Alzheimer disease. Proc Natl Acad Sci U S A. 2009; 106:1614–1619. [PubMed: 19164579]
3. Georgopoulos AP, Karageorgiou E, Leuthold AC, Lewis SM, Lynch JK, Alonso AA, Aslam Z, Carpenter AF, Georgopoulos A, Hemmy LS, Koutlas IG, Langheim FJ, McCarten JR, McPherson SE, Pardo JV, Pardo PJ, Parry GJ, Rottunda SJ, Segal BM, Sponheim SR, Stanwyck JJ, Stephane M, Westermeyer JJ. Synchronous neural interactions assessed by magnetoencephalography: a functional biomarker for brain disorders. J Neural Eng. 2007; 4:349–355. [PubMed: 18057502]
4. Schoffelen JM, Gross J. Source connectivity analysis with MEG and EEG. Human Brain Mapping. 2009; 30:1857–1865. [PubMed: 19235884]
5. Gross J, Kujara J, Hämäläinen M, Timmermann L, Schnitzler A, Salmelin R. Dynamic imaging of coherent sources: Studying neural interactions in the human brain. Proceedings of National Academy of Science. 2001; 98:694–699.
6. Belardinelli P, Ciancetta L, Staudt M, Pizzella V, Londei A, Romani NBGL, Braun C. Cerebro-muscular and cerebro-cerebral coherence in patients with pre- and perinatally acquired unilateral brain lesions. NeuroImage. 2007; 37:1301–14. [PubMed: 17669666]
7. Guggisberg AG, Honma SM, Findlay AM, Dalal SS, Kirsch HE, Berger MS, Nagarajan SS. Mapping functional connectivity in patients with brain lesions. Annals of Neurology. 2007; 63:193–203. [PubMed: 17894381]
8. Mantini D, Perucci MG, Gratta CD, Romani GL, Corbetta M. Electrophysiological signatures of resting state networks in the human brain. Proc Natl Acad Sci U S A. 2007; 104:13170–13175. [PubMed: 17670949]
9. Astolfi, L.; Babiloni, F. Estimation of Cortical connectivity in Humans. New York: Morgan & Claypool Publishers; 2008.
10. Miltner WHR, Braun C, Arnold M, Witte H, Taub E. Coherence of gamma-band EEG activity as a basis for associative learning. Nature. 1999; 397:434–436. [PubMed: 9989409]
11. Nunez PL, Srinivasan R, Westdorf AF, Wijesinghe RS, Tucker DM, Silberstein RB, Cadusch PJ. EEG coherency I: statistics, reference electrode, volume conduction, Laplacians, cortical imaging, and interpretation at multiple scale. Electroenceph Clin Neurophysiol. 1997; 103:499–515. [PubMed: 9402881]
12. Sekihara, K.; Nagarajan, SS. Adaptive spatial filters for electromagnetic brain imaging. Berlin, Heidelber: Springer-Verlag; 2008.
13. Nolte G, Wheaton OBL, Mari Z, Vorbach S, Hallett M. Identifying true brain interaction from EEG data using the imaginary part of coherency. Clinical Neurophysiology. 2004; 115:2292–2307. [PubMed: 15351371]

14. Hinkley LB, Owen JP, Fisher M, Findlay AM, Vinogradov S, Nagarajan SS. Cognitive impairments in schizophrenia as assessed through activation and connectivity measures of magnetoencephalography (meg) data. Frontiers in Human Neuroscience. 2009; 3:73. [PubMed: 21160543]
15. Martino J, Honma SM, Findlay AF, Guggisberg AG, Berger MS, Kirsch HE, Nagarajan SS. Resting functional connectivity in patients with brain tumors in eloquent areas. Annals of Neurology. in press.
16. Sarvas J. Basic mathematical and electromagnetic concepts of the biomagnetic inverse problem. Phys Med Biol. 1987; 32:11–22. [PubMed: 3823129]
17. Dalal SS, Guggisberg AG, Edwards E, Sekihara K, Findlay AM, Canolty RT, Berger MS, Knight RT, Barbaro NM, Kirsch HE, Nagarajan SS. Five-dimensional neuroimaging: Localization of the time-frequency dynamics of cortical activity. NeuroImage. 2008; 40:1686–1700. [PubMed: 18356081]
18. Fox MD, Raichle ME. Spontaneous fluctuations in brain activity observed with functional magnetic resonance imaging. Nature reviews neuroscience. 2007; 8:700–711.
19. Dalal SS, Zumer JM, Agrawal V, Hild KE, Sekihara K, Nagarajan SS. NUTMEG: A neuromagnetic source reconstruction toolbox. Neurol Clin Neurophysiol. 2004; 30:52. [PubMed: 16012626]
20. Theiler J, Eubank S, Longtin A, Galdrikian B, Farmer JD. Testing for nonlinearlity in time series: the method of surrogate data. Physica D. 1992; 58:77–94.
21. Faes L, Pinna GD, Porta A, Maestri R, Nollo G. Surrogate data analysis for assessing the significance of the coherence function. IEEE Trans Biomed Eng. 2004; 51:1156–1166. [PubMed: 15248532]
22. Benjamini Y, Hochberg Y. Controlling the false discovery rate: a practical and powerful approach to multiple testing. J R Stat Soc B. 1995; 57:289–300.
23. Nichols TE, Hayasaka S. Controlling the familywise error rate in functional neuroimaging: a comparative review. Statistical Methods in Medical Research. 2003; 12:419–446. [PubMed: 14599004]

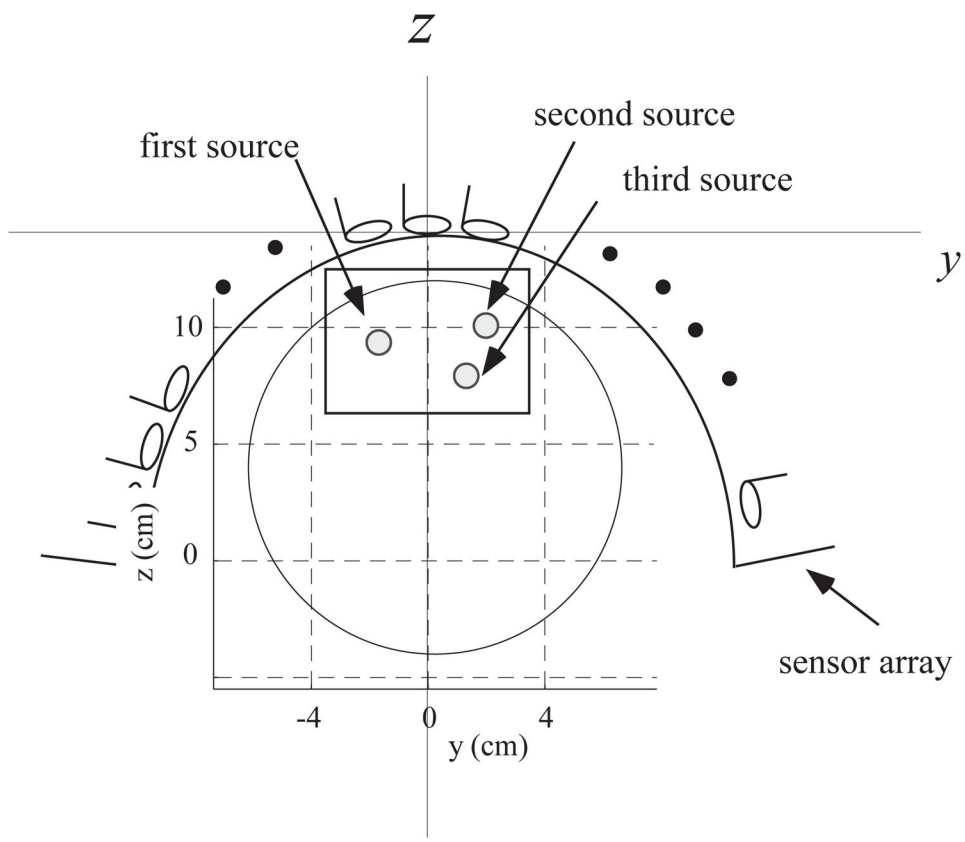


**Figure 1.**

The coordinate system and source-sensor configuration used in the computer simulation. The coordinate origin was set at the center of the sensor coil located at the center of the array. The plane at $x = 0$ cm is shown. The large circle shows the cross-section of the sphere used for the forward calculation, and the small circles show the locations of the three sources. The square shows the region for which reconstruction results are shown in Figs. 3–6.

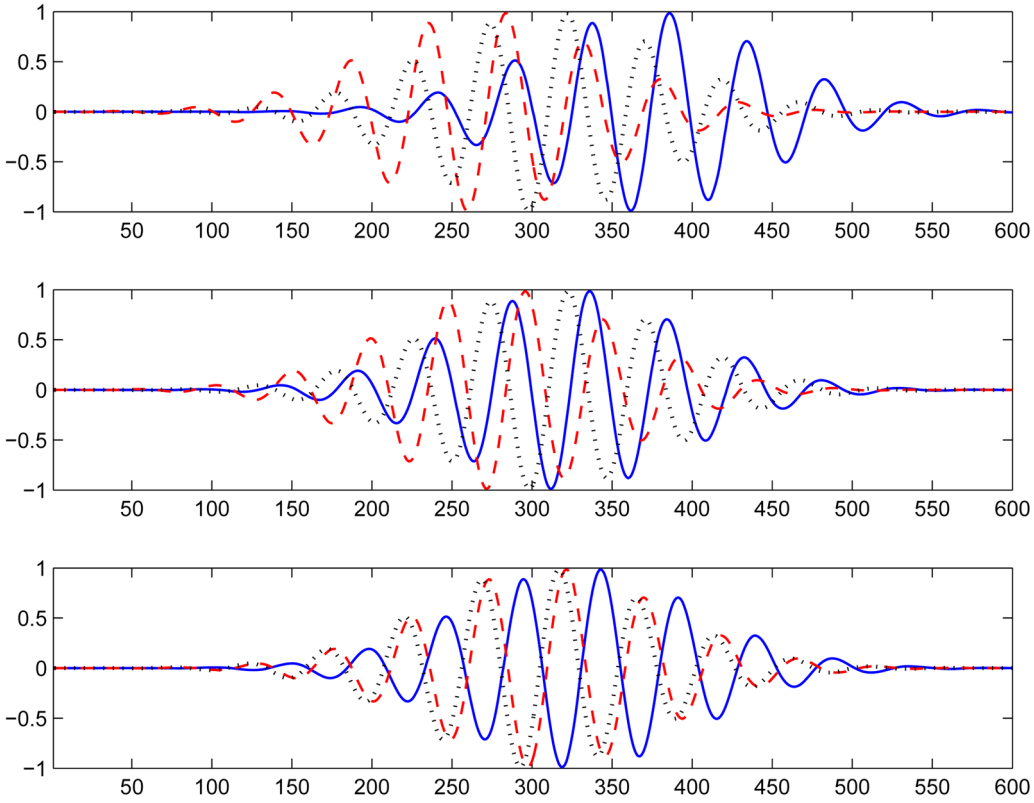


**Figure 2.**

The time courses assigned to the three sources in the computer simulation. The time courses in the top, middle, and bottom panels are those for the first, second, and the third sources. These time courses have trial-to-trial time jitters, and the time courses in the first three trials are shown. (The solid, broken, and dotted lines, respectively show the time courses for the first, second, and third trials.)

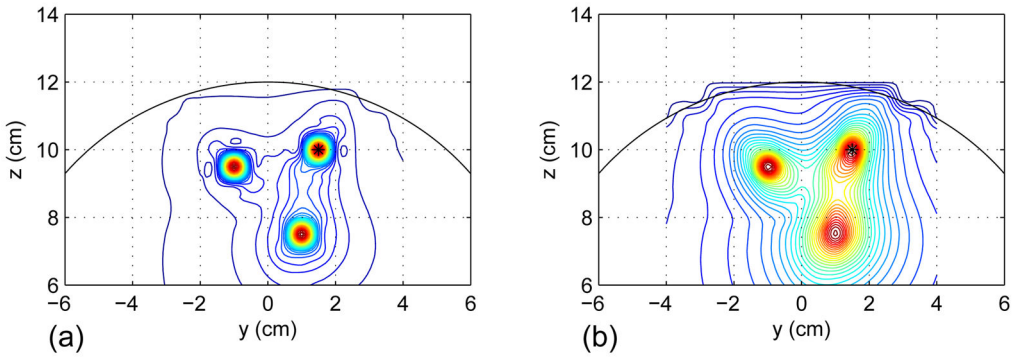


**Figure 3.**

Results of reconstructing source power distribution on the plane $x = 0$ cm. (a) SIR was set equal to 4.0. (b) SIR was set equal to 0.25. The asterisks show the location of the seed that was set for computing the coherence images shown in Figs. 4 and 5.

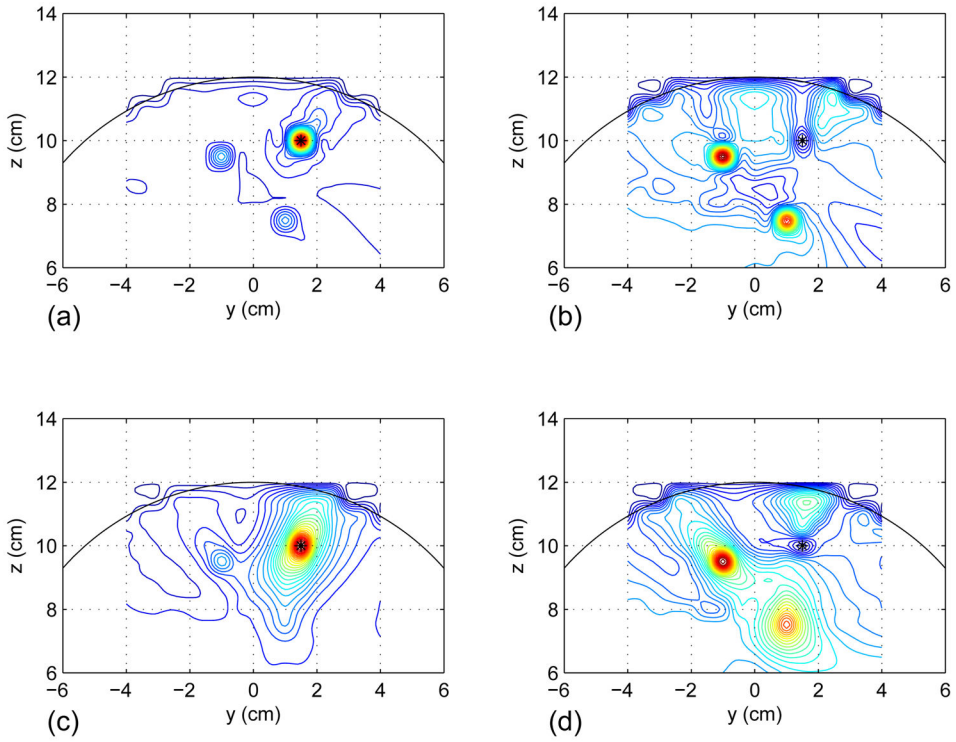


**Figure 4.**

Results of imaging the source coherence on the plane $x = 0$ cm. The seed was set at the second source location indicated by the asterisk. (a) Magnitude coherence image when SIR was set equal to 4.0. (b) Imaginary coherence image when SIR was set equal to 4.0. (c) Magnitude coherence image when SIR was set equal to 0.25. (d) Imaginary coherence image when SIR was set equal to 0.25.

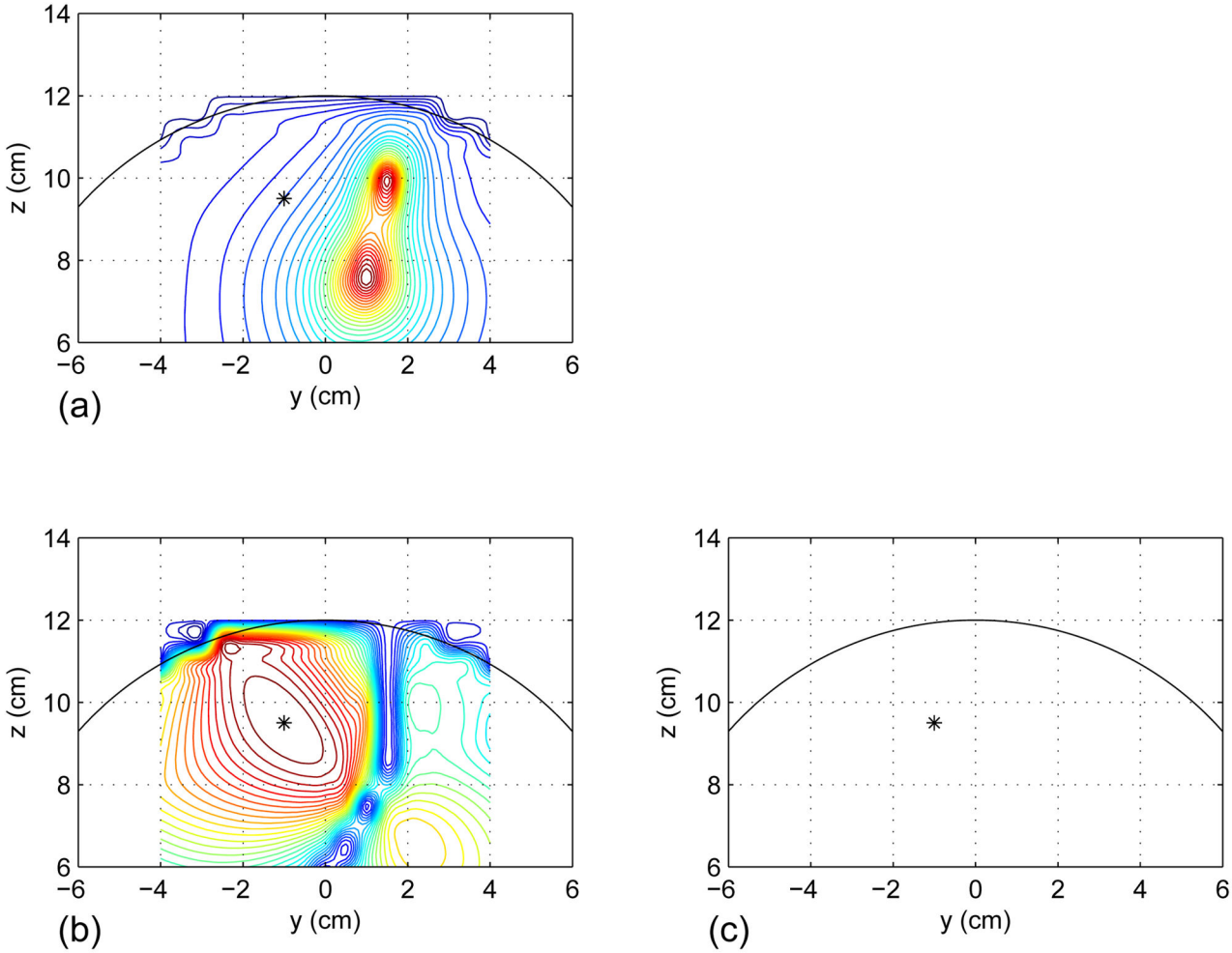


**Figure 5.**

Results of imaging the source coherence on the plane $x = 0$ cm when the seed was set at a location where no active source existed. The first source was made inactive, and the seed was set at the first source location indicated by the asterisks. (a) Reconstructed source power distribution. (b) Magnitude coherence image. (c) Imaginary coherence image.

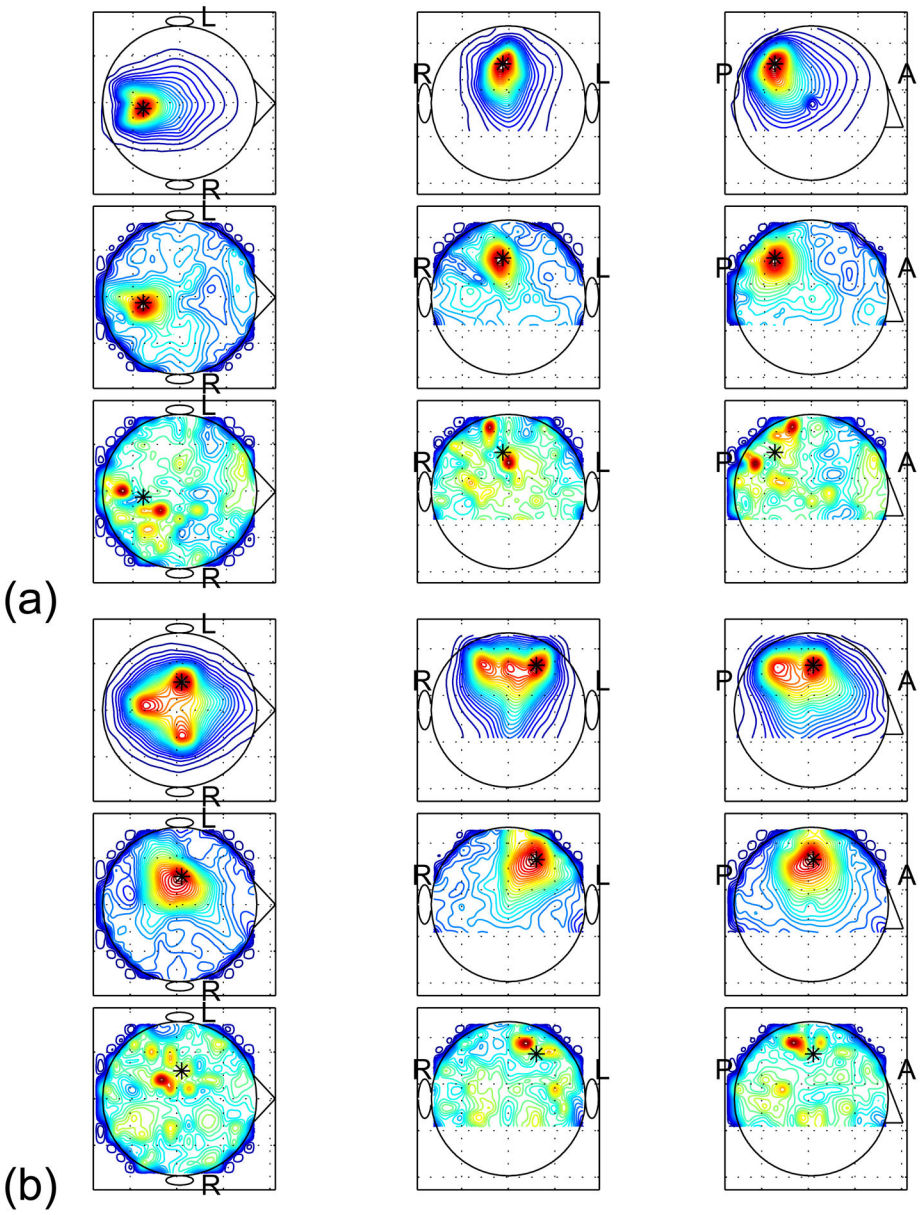


**Figure 6.**

Results of coherence imaging experiments performed using the resting-state MEG data from two subjects. (a) Results from the first subject and (b) results from the second subject. In each set of the results, the upper panels show the reconstructed source power distribution, the middle panels show the magnitude coherence image, and the bottom panels show the imaginary coherence image. The maximum-intensity projections onto the axial, coronal, and sagittal planes are shown respectively in the left-hand-side, middle, and right-hand-side columns. Letters L and R indicate the left and the right hemispheres, and the letters P and A indicate the posterior and the anterior directions. The asterisks show the location of the seed voxel.

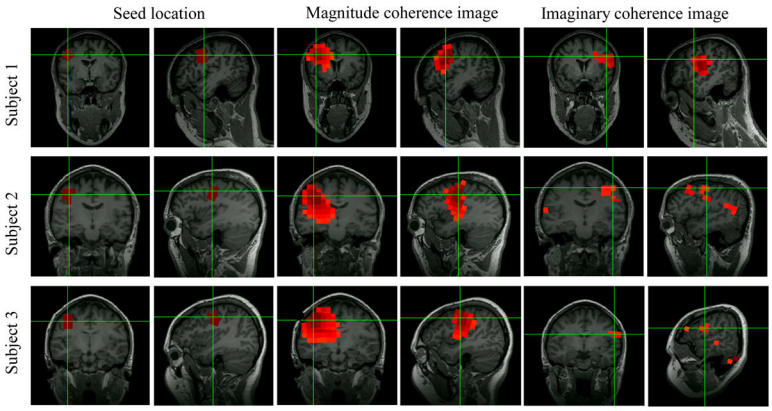


**Figure 7.**

Results of imaging beta-band coherence between the left and right primary motor cortices. The coherence images were obtained using the resting-state MEG data, and results for three subjects are shown. Two right-hand-side columns show the ten seed voxels in the pre-central gyrus. The two middle columns show the magnitude coherence images. The two right-hand-side columns show the imaginary coherence images. The results from the first, second, and the third subjects are respectively shown in the upper, middle, and bottom rows. These coherence images were obtained by averaging ten coherence images corresponding to the ten seed voxels.

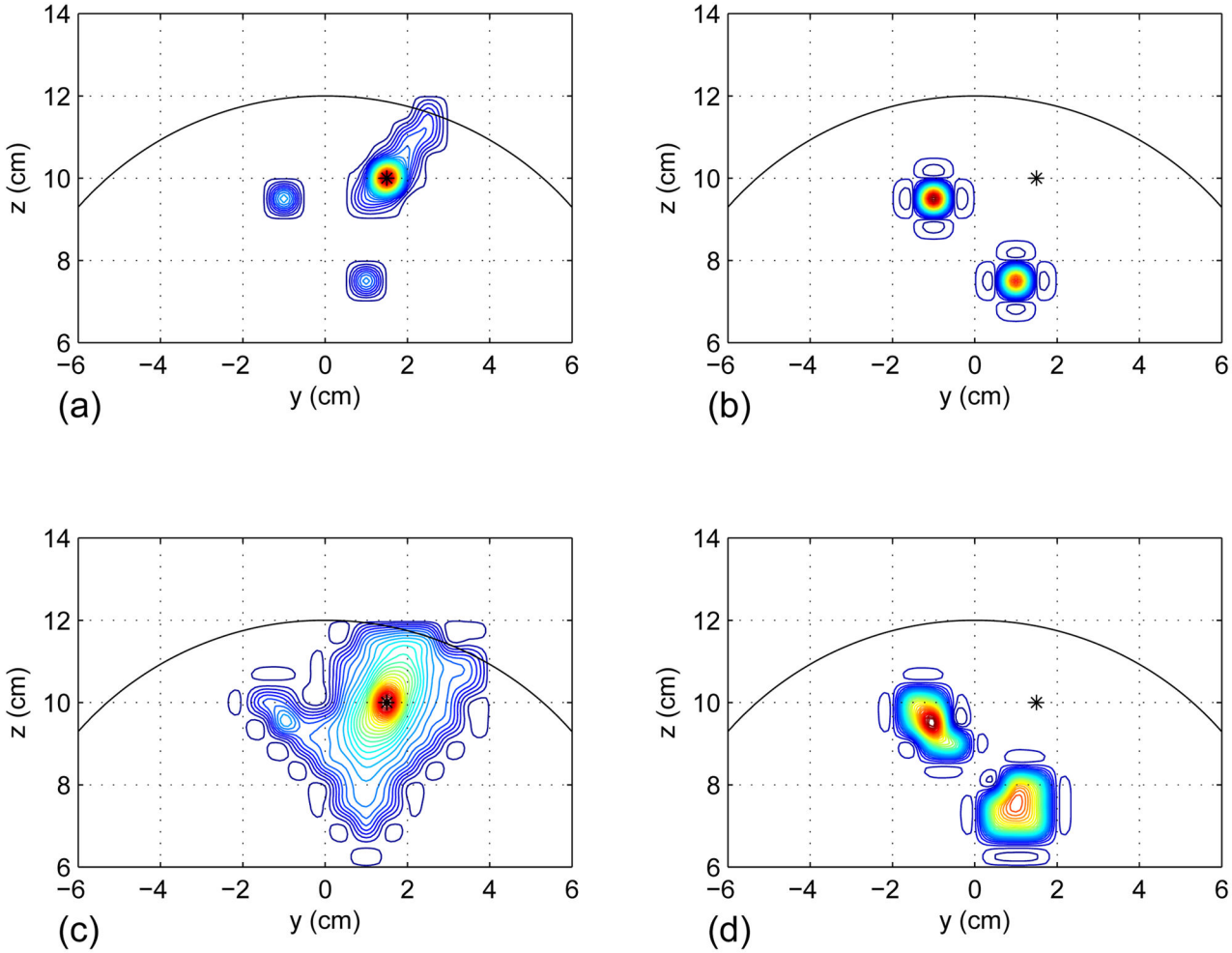


**Figure 8.**

Results of statistical thresholding for the computer simulation results shown in Fig. 4. Statistical threshold derived using the surrogate-data bootstrap method was applied and the statistical significance (the type one error rate) was set to 0.05. Results of imaging the source coherence on the plane $x = 0$ cm. The seed was set at the second source location indicated by the asterisk. (a) Magnitude coherence image when SIR was set equal to 4.0. (b) Imaginary coherence image when SIR was set equal to 4.0. (c) Magnitude coherence image when SIR was set equal to 0.25. (d) Imaginary coherence image when SIR was set equal to 0.25.